Journal Name

ARTICLE

Synergic effect of Bi, Sb and Te for the increased stability of bulk alloying anodes for sodium-ion batteries†

Receivedq 00th January 20xx,
Accepted 00th January 20xx

DOI: 10.1039/x0xx00000x

www.rsc.org/

M. W. Orzech,[a*] F. Mazzali,[a] J. D. Mcgettrick,[a] C. Pleydell-Pearce,[a] T. M. Watson, [a] W. Voice,[b] D. Jarvis,[b] and S. Margadonna,[a*]

Effective use of materials that undergo alloying reactions with sodium is hampered by the substantial volume changes that occur during cycling. One of the most common approaches to improve cycling stability is nanostructuring. However, the processes required for material's particle downsizing are hardly transferable to large scale production. To alleviate such problems, the ternary alloy $Bi_{0.25}Sb_{1.75}Te_3$ has been designed and its electrochemical performance investigated. The choice of system was driven by the large reversible capacities displayed by both Sb and Te coupled with the highly desirable fracture resistance of Bi. Indeed, micron-sized bulk powder of $Bi_{0.25}Sb_{1.75}Te_3$ showed high capacity retention (retaining 91% of the initial capacity after 100 cycles at 200 mA g^{-1}) and an excellent average coulombic efficiency (99.9% for 100 cycles), both of which are superior to those observed for the bi-component counterpart Sb_2Te_3 as bulk and nanosized forms. This behaviour indicates that a small substitution of Sb with Bi does have profound effects on the electrochemical performance. Even more compelling is the observation that enhanced performance and stability are observed when the active material is in the form of micron-sized powder and not when nanosized in a carbon composite. This behaviour is ascribed to the influence of particle size on the (de)sodiation reaction pathways and on the thickness and composition of the SEI passivation layer. The improved stability of the ternary alloy shows that careful optimization of multicomponent systems could lead to remarkable performance enhancement without the necessity of size confinement, opening the way to facile and low-cost electrode manufacturing.

Introduction

Sodium-ion batteries (SIBs) are currently heavily researched as a viable and sustainable technology for medium to large scale energy storage[1-5]. SIBs represent a low cost alternative to lithium-ion batteries (LIBs) for a number of reasons including: (i) the widespread availability of sodium, (ii) the possibility of using the cheaper and lighter aluminium current collector instead of copper, (iii) the electrochemical properties are close to those of lithium and (iv) drop-in solutions for their manufacturing can be easily adopted, as their cell assembly and production is analogous to LIBs.

In recent years, much research has focussed on the development of highly performing electrodes for SIBs. The negative electrode is, currently, one of the most troublesome components, since typical graphitic carbons employed in LIBs are inactive with sodium. Some disordered carbons, i.e. hard carbon, have been proposed, as they approach the specific capacity and stability displayed by graphite anodes in LIBs[1–3]. However, the volumetric capacity and Coulombic efficiency of carbon based anodes are low and, in addition, sodium is mainly stored below ~0.1 V (vs Na/Na^+). At such low voltage, problems with sodium plating emerge, particularly at higher charging rates. This raises a number of issues related to the safe use of such electrodes in commercial cells.

Alloying elements from groups 14-16 have been intensively studied as anodes for SIBs. They possess large theoretical gravimetric capacity as they form phases with high sodium content such as $Na_{15}Sn_4$ (847 mAh g^{-1}), Na_3Sb (660 mAh g^{-1}), Na_3Bi (385 mAh g^{-1}) or Na_2Te (420 mAh g^{-1}) and operate at higher and safer potential. However, their cyclic stability is hindered by huge volume changes causing pulverisation of the active material and loss of electrical contact with the current collector as well as continuous reconstruction of the solid electrolyte interphase (SEI) passivation layer. A number of different strategies have been developed to overcome such issues. Very high focus was put on the design of nanostructured alloy based anodes, usually embedded with some kind of carbon matrix. This approach has been extremely successful and high capacities as well as long cycle stabilities

[a] College of Engineering, Swansea University, Fabian Way, Crymlyn Burrows, Swansea SA1 8EN, UK
[b] Gervaux Ltd., West Bridgford, Nottingham, NG2 5JB, UK.
†Electronic Supplementary Information (ESI) available. See DOI: 10.1039/x0xx00000x

have been achieved. However, from the practical point of view, the synthetic procedures involved in the preparation of such materials are unlikely to be transferred to large scale production due to the their cost and complicated processing . Moreover, nanostructured materials have large specific surface area and low tap density, which reflects in large irreversible capacity loss during the formation of the SEI layer and low volumetric energy density. On the other hand, bulk materials are easy to manufacture in large scale and benefit from lower surface area and higher tap density. Therefore, more focus on low-cost, efficient and stable bulk electrode materials is needed for the prompt commercialisation of SIBs.

Another strategy to accommodate huge volume changes upon cycling, which is commonly used in conjunction with nanostructuring, involves the design of suitable alloys, where different constituents can serve as mutual self-support to suppress volume changes[4]. A careful choice of the components in the alloy-based anode can result in a much improved cycle stability and capacity retention. Indeed, several binary and ternary alloys have been reported to exhibit improved cycling stability, such as Sn-Sb[5], Sn_4P_3[6,7], Bi-Sb[8], Sb_2S_3[9], $NiSe_2$[10], $Bi_{0.94}Sb_{1.06}S_3$[11], $CuSbS_2$[12], Sn-Ge-Sb[13], Sn-Bi-Sb[4] and Sn_5SbP_3/C[14]. In all cases, the performance of the alloys is enhanced as compared to their single element counterparts. A recent report on Sn-Bi-Sb thin alloy films (100 nm in thickness) showed very clearly the beneficial effects of alloying small amounts of Bi and Sn (10 at%) with Sb (80 at%), which resulted in single-phase microstructure[4]. Improvement in the performances of the ternary alloys was explained in terms of solid solution strengthening and a more stepwise sodiation mechanism. Interestingly, the performance was not influenced by the grain size in the nanoscale range.

Within this context, our aim was to design an alloy based anode material which is stable in its bulk micronsized form to avoid any nanostructuring step in the electrode processing. To achieve this goal, it is necessary to make use of the beneficial effects of multicomponent alloys, such as solid solution strengthening, mutual buffering and gradual sodiation process. Furthermore, the selection of components is crucial as enhanced stability must be achieved without compromising on gravimetric capacity. Our choice fell on a ternary alloy comprising Sb, Te and Bi which were all already studied as single or binary alloys[15–20]. Sb has been widely researched and when nanostructured shows remarkable stability and rate capability[19,21–23]. On the other hand, Bi displays lower specific capacity but exhibits extraordinary mechanical properties upon sodiation[24] and a fairly high capacity retention[25,26]. Sb and Bi adopt the same crystal structure and are able to form $Bi_{1-x}Sb_x$ solid solution for $0 < x < 1$. They are active against sodium in very similar voltage potential and therefore another element, with quite different operating voltage, is necessary to take full advantage of the benefits of mutual buffering and gradual sodiation. Recent studies have demonstrated that complex Te-nanocomposites could reach outstanding cycling stability of 90% capacity retention at the 1000th cycle[27,28]. Te is electrochemically active at a higher potential than Sb, and therefore their combination can effectively alleviate the reciprocal volume changes during cycling. However, the binary alloy Sb_2Te_3, which is a well-known thermoelectric and a much studied topological insulator, has been recently studied as anode for SIBs. Nanocrystallites (sized 5-8 nm) embedded in carbon matrix showed interesting properties displaying a reversible gravimetric capacity of 373 mAh g^{-1} over 50 cycles[29]. However, our preliminary electrochemical testing, which extended to more than 50 cycles, has shown less than desirable cycling stability of the Sb_2Te_3 alloy both in bulk and in its nanosized forms. A third component therefore should be added to improve performance. The obvious choice would be to use Bi, considering its desirable mechanical properties, which can improve electrode stability without hampering its gravimetric capacity. Additionally, Bi forms stable solid state solution with both Sb and Sb_2Te_3. As a recent study[4] showed, the Bi addition is most efficient if it constitute of 10% to 20% in relation to Sb in alloy. Therefore, we produced the designed ternary alloy $Bi_{0.25}Sb_{1.75}Te_3$ (12.5 at% of Bi to 87.5 at% of Sb) and studied its suitability as anode material for SIBs both as bulk material and as a carbon nanocomposite. Electrochemical testing has shown that the performance of $Bi_{0.25}Sb_{1.75}Te_3$ is far superior to the binary Sb_2Te_3 alloy with the same particle size demonstrating that a relatively small replacement of Sb with Bi significantly improves electrode stability. Very importantly, the direct evaluation of micron-sized powder vs carbon nanocomposite reveals that the latter displays an inferior capacity retention and rate capability. These results contradict the general understanding that structural confinement is an essential requisite for alloying electrode stability and prove that superior performances can be achieved in bulk alloys.

To elucidate the mechanism behind this intriguing behaviour *ex situ* X-ray powder diffraction (XRD), X-ray photoelectron spectroscopy (XPS) and electron microscopy (SEM and TEM) measurements were performed. Our results showed that the reaction pathways occurring during (de)sodiation are dependent on the original particle size of the alloy. Additionally, the SEI layer on the nanocomposite is thicker and consists of more inorganic species than in micron-sized alloy. These findings show that smart design of alloys could be a facile alternative to nanostructuring for performance improvement of anode materials, which would open the path to an inexpensive electrode processing.

Experimental

Materials synthesis

The $Bi_{0.25}Sb_{1.75}Te_3$ alloy supplied by Gervaux Ltd. was in the form of a pellet and used as received. Micron-sized powder (herein referred as bulk-BST) was obtained by crashing the pellet using a Fritsch Pulverisette 23 for 5 min at 50 Hz. To prepare the carbon composite (herein referred as nano-BST/C), the resulting powder was further milled with carbon black (Super P, Timcal) in 70:30 wt% ratio, respectively. Powders were sealed in stainless steel jar under Ar atmosphere and ball milled at 300 rpm for 12 h using high energy planetary ball mill Pulverisette 5. The ball to powder

ratio was 15:1. The obtained nanopowder was stored under Ar to avoid oxidation. The Sb_2Te_3 and Sb_2Te_3/C materials were synthesized in the same manner.

Materials Characterisation

X-ray powder diffraction (XRD) patterns of materials and electrodes were measured on a Bruker D8 Advance diffractometer with a Cu Kα radiation source (λ = 1.5406 Å). The XRD patterns were collected over the range of 10–80° by keeping the step size of 0.01° at a scan rate of 7 s per step. For the *ex situ* measurements electrode materials were removed from the current collector and sealed in glass capillaries under Ar atmosphere.

Scanning electron microscopy (SEM) imaging was performed with a ZEISS Evo scanning electron microscope. The accelerating voltage was 15 kV and the working distance was ~10 mm. The electrodes for SEM imaging were extracted from half-cells after the first cycle, washed with propylene carbonate and transferred to SEM chamber with negligible exposure to air. High-resolution transmission electron microscopy (HRTEM and STEM) images were obtained with a FEI Talos, operating at 200 kV. For the *ex situ* imaging, a TEM grid loaded with Bi-Sb-Te/C nanocomposite was pressed against the electrode[30]. After electrochemical cycling, the TEM grid was carefully removed and rinsed with propylene carbonate. The grid was loaded on TEM holder in glove box and transferred under Ar protection to microscope chamber without any exposure to air.

The surface analyses were performed by means of X-ray photoelectron spectroscopy (XPS, Kratos Axis Supra) using focused monochromatic 225W Al Kα radiation (*hv* = 1486.6 eV). The high resolution peaks were recorded with constant pass energy of 40 eV. The analysis area was limited by an aperture to a 110 µm diameter circle. To minimize charging effects, the Kratos charge neutralization system was used. For etching monatomic Ar^+ beam with an applied voltage of 5 keV was employed. Photoelectron spectra were fitted with Casa XPS software with Shirley backgrounds and 30% Gaussian, 70% Lorentzian curves. The binding energy (BE) scale was calibrated from the adventitious carbon using the C 1s peak at 284.8 eV. Quantification was performed using the Kratos relative sensitivity factor (R.S.F.) library.

Electrochemical characterisation

The micron-sized powder was mixed with Super P (Timcal Ltd.) and sodium carboxymethyl cellulose (CMC) binder (in a weight ratio of 70:15:15) in de-ionized water to form a homogenous slurry. The nanocomposite material was mixed with CMC binder only in weight ratio 90:10. Lower content of binder is chosen to keep similar loading of active material in both samples, thus matching whole electrode volume change upon cycling. The slurries were then coated on Al foil, pressed and dried in vacuum oven at 80°C overnight. All electrodes were 12.5 mm diameter discs. Na metal was used as both counter and reference electrode. Electrochemical performances were evaluated with standard CR2032 coin cells. The electrolyte used was 1 M $NaPF_6$ (99+%, Alfa Aesar) solution in a mixture of ethylene carbonate (anhydrous, 99%, Sigma) and propylene carbonate (anhydrous, 99.7%, Sigma) in 1:1 volume ratio with 5wt% fluorinated ethylene carbonate (99%, Sigma) additive. FEC additive is known to improve the stability of the SEI layer, hence enhance cycle life[31–34]

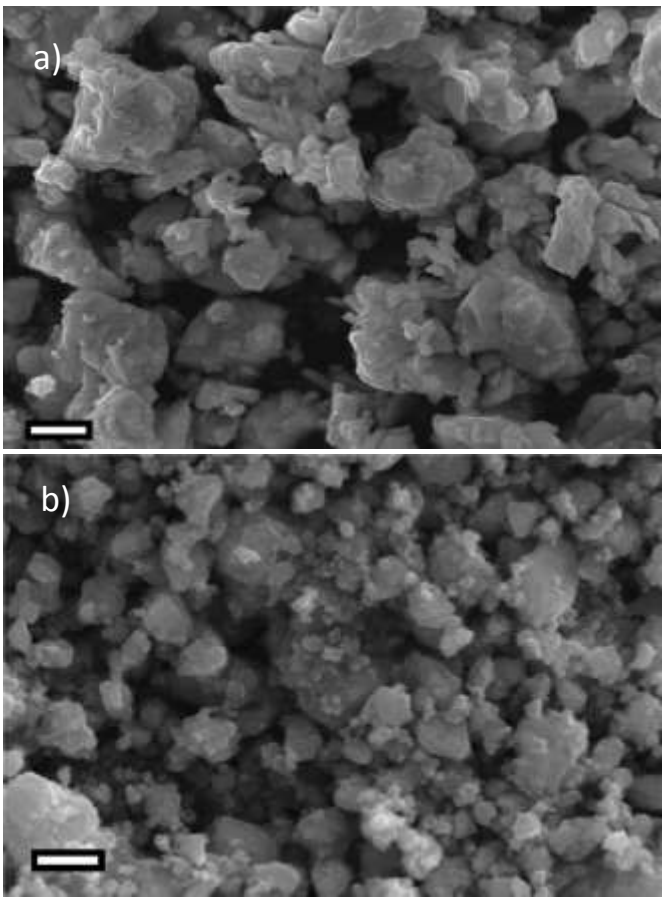

Figure 1. Morphology of bulk-BST and nano-BST/C. SEM images of $Bi_{0.25}Sb_{1.75}Te_3$ before (a) and after ball milling with carbon (b). Scale bars are 2 µm.

Whatman glass-fiber separators were used. The cells were assembled in an argon-filled glovebox with O_2 and H_2O levels less than 0.1 ppm and aged for 2 h before tests to ensure full absorption of electrolyte into the electrodes. Galvanostatic cycling was performed in a voltage range of 0.01 V to 2 V vs Na/Na^+ using a Bat-Small battery cycler (Astrol). Cyclic voltammetry was performed in the voltage range of 0.01 - 2 V at a scan rate of 0.1 mV s^{-1} using Bio-Logic VMP3 potentiostat.

Results and discussion

Materials characterisation

The room temperature X-ray powder diffraction profile of the as received ternary alloy with nominal composition $Bi_{0.25}Sb_{1.75}Te_3$ (bulk-BST), can be readily indexed with a single rhombohedral phase characteristic of both Sb_2Te_3 and Bi_2Te_3 (space group R-3m) with refined lattice constants a = 4.2842(1) Å and c = 30.433(2) Å (Fig. 2a and S1). The crystal structure comprises stackings of three "quintuple layers" [Te(I)-Bi/Se-Te(II)-Bi/Se-Te(I)-building blocks with Te(I) and Te(II) denoting

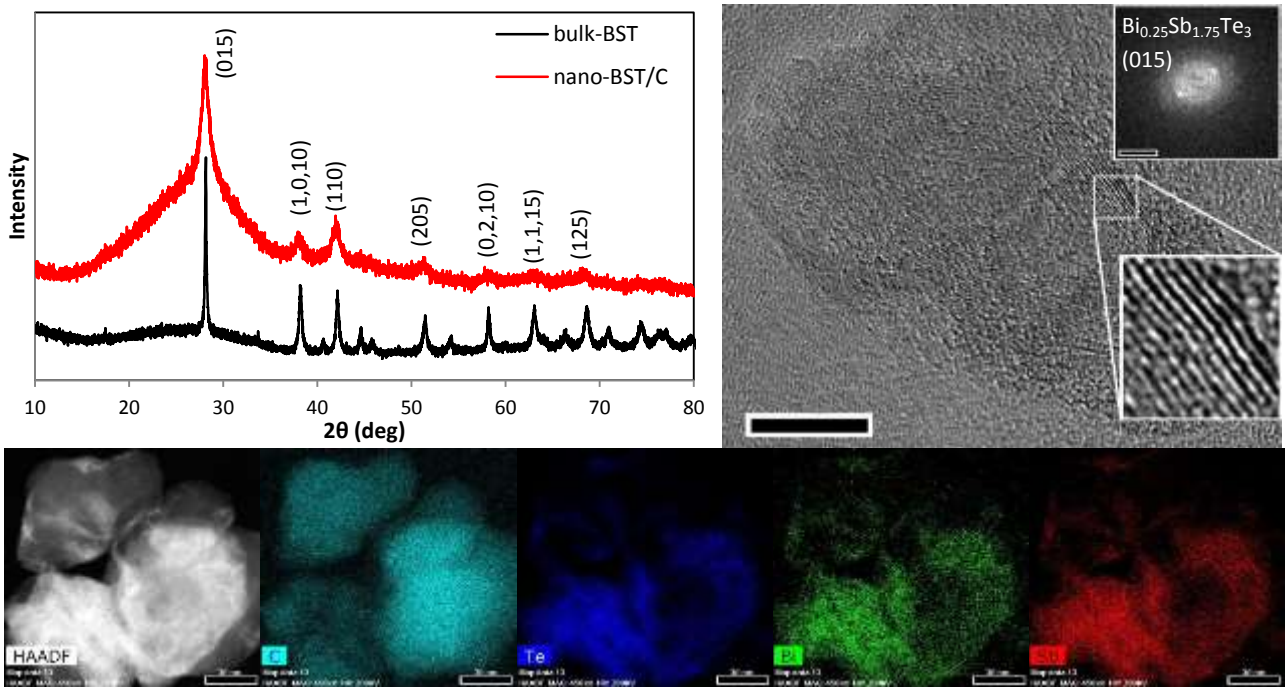

Figure 2. Structural characterisation of bulk-BST and nano-BST/C. (a) X-ray diffraction pattern bulk-BST (black) and nano-BST/C (red). (b) HRTEM image of nano-BST/C crystallites (enlarged) embedded in carbon matrix (scale bar, 10 nm). The corresponding FFT is shown in the inset (scale bar, 5 nm^{-1}). (c) Dark field image of nano-BST/C and corresponding EDS maps (scale bar, 30 nm).

two different coordinations of the tellurium atoms. Bi and Sb statistically occupy the *6c* Wyckoff position (0, 0, 0.399) with refined fractional occupancies of 0.12(1) and 0.88(1) respectively. The resulting stoichiometry of the ternary alloy is $Bi_{0.24(1)}Sb_{1.76(1)}Te_3$ which is well in line with its nominal composition (Table S1).

Diffraction profiles of the original powder after ball milling with carbon show that the rhombohedral layered structure is preserved with no changes in lattice dimension (Fig. 2a). However, differences are observable in the peak widths which have now become much larger indicating smaller crystallite size. Application of the Sherrer equation resulted in an average crystallite size of 6.8 nm. Ball milling does not induce phase separation or the formation of spurious phases. The presence of carbon is directly detectable by the large amorphous background between 2θ = 15° and 35°.

The morphological characteristics of both materials, bulk powder and carbon nanocomposite are shown in Fig. 1. From scanning electron microscopy (SEM) images (Fig. 1a,b) the effect of high energy mechanical milling (HEMM) on particle size can be easily determined. In the bulk-BST powder (Fig. 1a) the average particle size is 2 µm and the shape observed is typical for layered crystals. On the other hand, after ball milling with carbon the nanocomposite formed more irregularly shaped agglomerates with the average size reduced to 80 nm. Fig. 2b shows the HRTEM image of nano-BST/C with Bi-Sb-Te crystallites sizes ranging between 5 and 15 nm consistent with the results of the Sherrer line broadening analysis. The d-spacing obtained from Fast Fourier transform (FFT) pattern of the selected area corresponds to the (110) plane of $Bi_{0.25}Sb_{1.75}Te_3$. High angle annular dark field (HAADF) STEM image and energy dispersive spectroscopy (EDS) elemental mapping showed that the alloy particles are uniformly covered by a 15 nm thick carbon layer (Fig. 2c). The absence of carbon in bulk-BST and its presence in nano-BST/C were further confirmed by Raman spectroscopy (Fig. S8)

Electrochemical performance

The electrochemical performance of the materials was evaluated through galvanostatic charge/discharge cycling in the voltage window 0.01 – 2.0 V with current density 200 mA g^{-1} (Fig. 3a). The bulk-BST anode showed initial discharge capacity of 536 mAh g^{-1}, which is slightly higher than the weighted average of theoretical capacities of elements (496 mAh g^{-1}). This excess capacity is attributed to the SEI layer formation. First charge capacity reached 450 mAh g^{-1} giving high overall first cycle efficiency of 84%. After 100 charge/discharge cycles the high capacity of 406 mAh g^{-1}, i.e. 91% of initial capacity is retained. The excellent average Coulombic efficiency of 99.9% after initial cycle suggests good utilisation of electrode in a full cell.

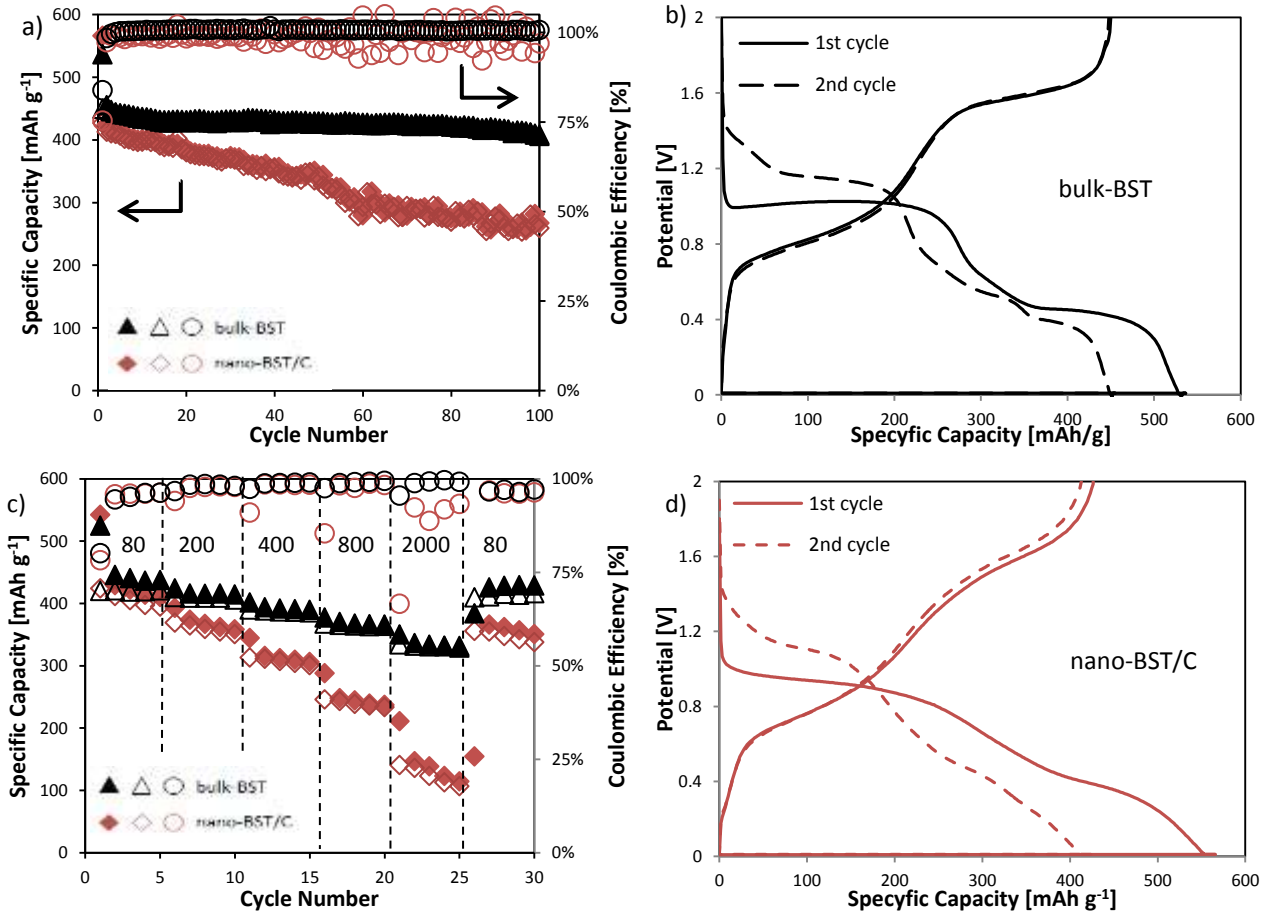

Figure 3. Electrochemical performance of bulk-BST and nano-BST/C. (a) Galvanostatic cycling of bulk-BST and nano-BST/C with current density 200 mA g^{-1} in a potential window 0.01 – 2.0 V vs Na/Na^+ and corresponding charge-discharge curves of (b) bulk-BST and (d) nano-BST/C anodes at first (solid) and second cycle (dashed). (c) Rate capability of anodes at different current densities (numbers in mA g^{-1}).

The ball milled material nano-BST/C showed slightly higher first discharge capacity of 566 mAh g^{-1} but displayed a much lower first cycle coulombic efficiency of 75% suggesting that, in this case, more electrolyte was decomposed to form a stable SEI layer. This behaviour is expected considering the larger surface area of the nanocomposite. Furthermore, nano-BST/C showed constant capacity fading of averaged 0.45% per cycle, which results in only 60% capacity retention after 100 cycles.

It is relevant to mention, at this point, that the performances of analogous electrodes consisting of micron and nanosized Sb_2Te_3 without Bi substitution, tested under identical conditions, show an opposite trend. In the case of bulk Sb_2Te_3 complete pulverisation and exfoliation of the anode from the current collector occurs within the first 10 cycles (Fig. S2). However, when the particles size is reduced and a nanocomposite with C is produced via high energy ball milling, the electrochemical response of Sb_2Te_3/C is much improved reaching a reversible capacity of 490 mAh g^{-1} at a current density of 200 mA g^{-1}. However, after about 50 cycles capacity quickly drops, revealing electrode instability and poor cycle life. These observations point towards a scenario where a small substitution of Bi has beneficial effects on the electrode stability which, very importantly, is modulated by particle size.

Figures 3b and 3d show charge-discharge curves of the first two cycles for both anodes. The initial discharge (charge) curve of bulk-BST displays two flat plateaus at 1.05 V (1.57 V) and 0.51 V (0.74 V). The higher voltage plateau can be ascribed to the reaction of Na with Te, while at the lower potential both Sb and Bi are active. In the subsequent cycle the sodiation plateau of Te shifts to 1.15 V and the plateau assigned to Sb and Bi splits into two at 0.54 V and 0.39 V. Moreover, a sloping region appears around 1.30 V. This shape is reflected in the nano-BST/C anode curves, even though the plateaus are more sloped and their exact potentials are harder to specify. This is typical of many amorphous or nanocrystalline alloy anodes, which often have voltage curves comprised of single-phase regions with significant amounts of polarization[35].

To further elucidate differences in performance between micron and nanosized ternary alloy anodes, rate capability measurements were conducted. The resulting charge/discharge capacity versus cycle number plot is presented on Fig. 3c. Average charge capacities of bulk-BST are 420, 409, 388, 365 and 331 mAh g^{-1}, and of nano-BST/C 406, 360, 307, 240 and 124 mAh g^{-1}, obtained at current densities of 80, 200, 400, 800 and 2000 mA g^{-1}, respectively. Even at as high current density as 2000 mA g^{-1} 80% of the bulk-BST

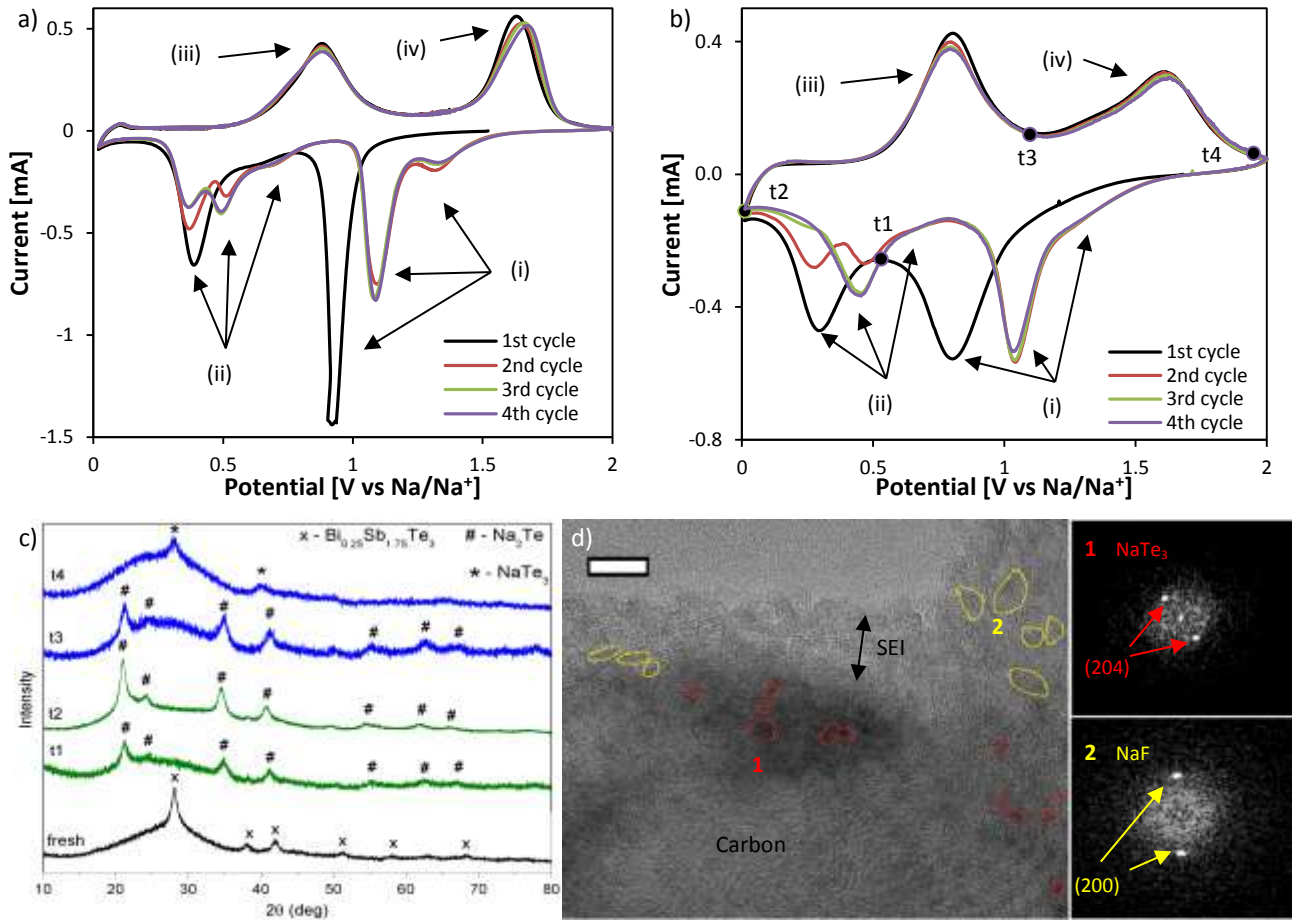

Figure 4. $Bi_{0.25}Sb_{1.75}Te_3$ electrodes de/sodiation mechanism. (a,b) First four CV scans with scan rate 0.1 mV s^{-1} of (a) bulk-BST vs Na, (b) nano-BST/C vs Na. (c) *Ex situ* X-ray diffractograms of nano-BST/C anode pristine (black) during sodiation (green) and desodiation (blue). (d) *Ex situ* TEM image of nano-BST/C at t4 (2 V) and corresponding FFT patterns (scale bar, 10 nm).

capacity is retained. This value is only 30% for the nano-BST/C. After deep cycling at 2000 mA g^{-1}, when the current rate is set back to 80 mA g^{-1}, the former electrode recovered a high charge capacity of 410 mAh g^{-1}, which shows the promising structural stability of the bulk ternary alloy at high currents. These results demonstrate the superior rate performance of the bulk-BST anode at higher current densities. Again, this goes against the common understanding that nanostructures, due to shorter diffusion paths, which are beneficial for fast Na-ion transfer and an increased number of reaction sites, offer improved rate capabilities.

De/sodiation mechanism

To better understand the charge-discharge process of the ternary alloy, the electrochemical behaviour of both anodes were evaluated using cyclic voltammetry (CV) at a scan rate of 0.1 mVs^{-1}. Results are shown in Fig. 4a and 4b. Moreover, to further elucidate the de/sodiation mechanism, *ex situ* XRD measurements of both anodes were taken at the potentials t1, t2, t3 and t4 (Fig. 4c). The charge/discharge mechanism can be separated into two stages, i.e. activity of tellurium at higher potentials and activity of Sb and Bi at lower potentials. On the CV scan the first stage is represented by the peaks (i) and (iv) indicated by arrows, while those noted (ii) and (iii) are ascribed to reactions of Sb and Bi.

The CV profile of the first cycle of bulk-BST electrode is quite different from those of the subsequent cycles, suggesting an activation process during the first discharge (Fig. 4a). It shows the presence of two peaks, one (i) around 0.93 V and another (ii) at ~0.38 V. Additionally, a low intensity broad feature around 0.75 – 0.55 V can be identified. The former peak can be associated to intercalation of Na^+ ions into the van der Walls gaps of the rhombohedral structure, which leads to breaking of $Bi_{0.25}Sb_{1.75}Te_3$ structure and formation of the SEI layer. Subsequently, the conversion reaction occurs, leading to the formation of crystalline Na_2Te. Presence of this phase was confirmed by *ex-situ* XRD measurements (Fig. S3 and S4) and it is in agreement with what has been reported in the literature for Te-based and Sb_2Te_3 anodes[28,29]

In the second stage of discharge Sb plays dominant role, as content of Bi is relatively small. The shape of the (ii) part of the CV scan of the bulk-BST resembles shape of previously reported second - rather than first - sodiation profile of Sb anodes[18,36,37]. Allan et al. showed that pure antimony upon Na insertion forms several amorphous phases, i.e. Na_1Sb and

$Na_{1.7}Sb$, with final $Na_{3-x}Sb$[37]. In the presented dQ/dE plot the broad feature around 0.7 V is ascribed to insertion of Na into amorphous Na_1Sb to form also amorphous $Na_{1.7}Sb$. The following peak at 0.45 V reflects the amorphous $Na_{3-x}Sb$ phase formation[18,36,37]. Similarly, in the bulk-BST electrode, the broad feature can be attributed to the reaction of a small amount of partly sodiated Sb. However, the following peak is shifted to the lower potential of 0.38 V, suggesting some different mechanism occurring. After breaking of the starting $Bi_{0.25}Sb_{1.75}Te_3$ structure the Sb an Bi can form solid solution where intrinsic stresses are higher than in pure metals[38]. A recent work on Sn-Bi-Sb alloys showed solid solution modification of the Sb chemical potential and stress induced voltage changes[4]. The lower than expected potential of cathodic peak strongly suggest that $Sb_{1-x}Bi_x$ solid solution is formed and consequently sodiated to $Na_ySb_{1-x}Bi_x$ ($y \leq 3$) – a mechanism analogous to lithiation of Si-Ge alloys[39,40]. Both Sb and Bi form hexagonal Na_3M structure upon discharge, therefore the formation of sodiated solid solution is possible.

The oxidation peaks at 0.84 V (iii) and at 1.65 V (iv) relate to sodium extraction from Sb/Bi and Te respectively. After the first full cycle, the partly sodiated $NaTe_3$ phase can be clearly observed on the *ex situ* XRD diffraction profiles (Fig. S3). Additionally, small amount of Na_2Te remained in the electrode, indicating incomplete desodiation. This behaviour is similar to previously reported by Zhang et al. for bulk Te electrode[28].

In the second and subsequent scans the higher voltage reduction peak (i) splits into two features located at 1.34 V and 1.09 V. This phenomenon reveals a two-step sodiation mechanism of Te in the bulk Bi-Sb-Te alloy after the first cycle. The 1.34 V peak could be ascribed to intermediate Na_xTe phase formation, though it can't be clearly distinguished by means of *ex situ* XRD[28]. It is followed by further sodiation to Na_2Te at 1.09 V. In the second stage of discharge (ii) related to Sb and Bi significant changes in the CV profile can be observed. The broad feature is still present and shifts to slightly higher potentials due to relaxation of some stresses, thus lower overpotential. More importantly, new peak appears at 0.49 V, which is similar to pure Sb behaviour and can be ascribed to sodiation of $Na_{1.7}Sb$ to $Na_{3-x}Sb$[37]. This indicates segregation of some Sb from the solid solution. The peak at 0.38 V is still present and confirms existence of two antimony-based phases in electrode, i.e. segregated Sb and Sb-Bi solid solution. In the following cycles CV profile remains unchanged indicating good reversibility of bulk-BST anode.

The CV profile of the nano-BST/C differs from that of micron-sized material. First of all the peaks are broader and shifted, which is caused by higher overpotential in nanostructured electrodes, as mentioned before. The first stage - (i) and (iv) - related to Te activity shows no significant changes from bulk material. Additionally, the *ex situ* XRD measurements at t1 showed clear presence of the Na_2Te phase. However, at t4 only $NaTe_3$ was clearly detected, indicating more facile desodiation of nano-Te, in agreement with previous work of Zhang et al.[28] To further confirm the presence of $NaTe_3$ phase, *ex situ* HRTEM measurements of nano-BST/C electrode at fully charged state were performed (Fig. 4d). Amorphous carbon matrix with agglomerated nano-crystallites sized 2-4 nm of $NaTe_3$ can be seen. It should be mentioned that neither Na_2Te nor crystalline Sb-Bi was observed. Additionally, the electrode is covered with about 10-15 nm thick SEI layer composed of crystalline NaF and various amorphous phases.

Larger differences between the two materials can be observed in the lower voltage part (ii) of CV profile. Due to overpotential, the peaks are shifted, i.e. from 0.38 V in bulk-BST to 0.30 V in nano-BST/C and from 0.49 V to 0.45 V, respectively. Moreover, the former peak disappears after the third cycle. This indicates instability of solid solution in the nanostructured electrode (see ESI for a schematic description of the de/sodiation mechanism).

It has been previously reported that antimony-based electrodes, including Sb_2Te_3, form crystalline Na_3Sb[29,37] at full sodiation. The *ex-situ* experiments performed here never revealed the presence of this phase in any of tested anodes (Fig. 4c and S3). It has been shown that the presence of other elements and intrinsic stresses can deeply influence the sodiation mechanism and hinder the crystallisation of the fully sodiated Sb-phase[4,9,41,42]. Bi is active in the same potential region as Sb (0.4-0.6 V vs Na/Na^+) and forms NaBi and Na_3Bi phases[17,43]. However, again, Bragg peaks relative to these phases are not distinguishable in the *ex situ* diffraction profiles. It is known that the sodiated phases of Bi are metastable and can't be detected by *ex situ* measurements[16,26,43]. Although sodiation products of Sb and Bi cannot be identified by means of *ex situ* XRD due to amorphisation (Sb) or metastability (Bi), the specific capacity observed in the galvanostatic cycling is very close to the theoretical value, indicating full utilisation of all the three metallic components.

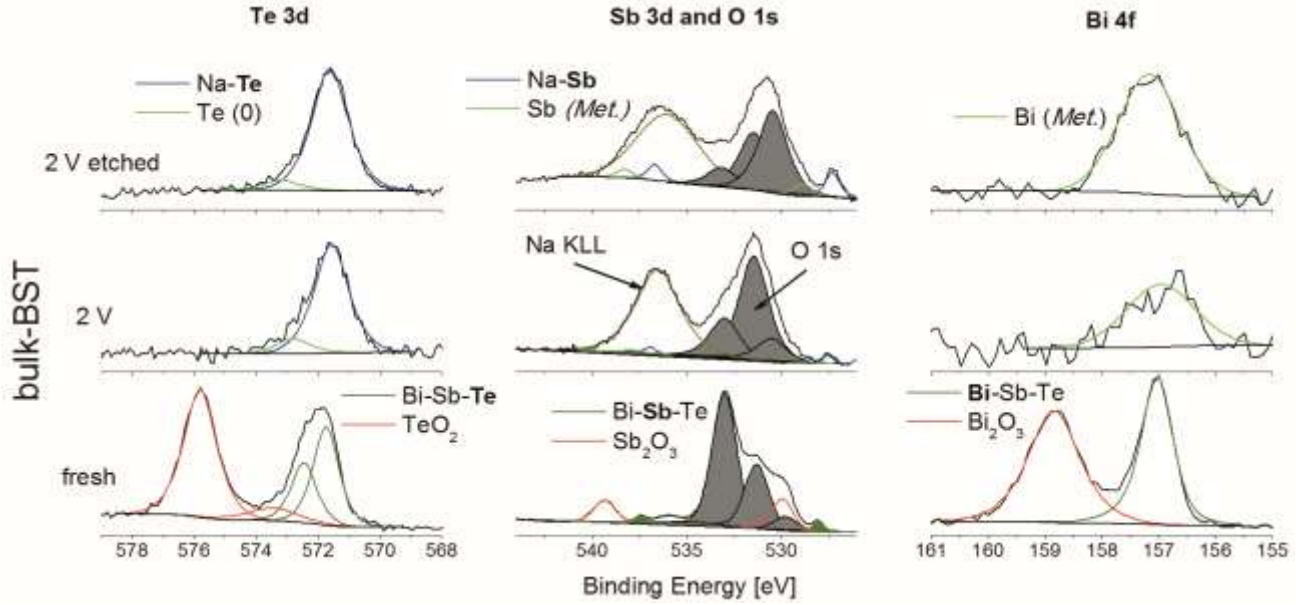

Figure 5. Surface analysis of fully charged bulk-BST electrode. *Ex situ* XPS plots of Te (3d), O (1s) & Sb (3d), and Bi (4f) envelopes.

It is worth to compare the reaction mechanisms of nano-BST/C with the recently reported results on the related system Sb_2Te_3-carbon nanocomposite that appears to undergo a recombination reaction to afford Sb_2Te_3 on desodiation[29]. This drastically differs from the behaviour of the ternary alloy where no signature of either the original phase or of Sb_2Te_3 is observed. It follows, that Bi plays an important role in determining the reaction pathways and consequent electrode performance.

Surface analysis

To further elucidate the effect of particle size on the electrochemical performance of the anode, *ex situ* XPS measurements of both electrodes, as coated and at fully charged state, were performed (Fig. 5 and S6). X-ray photoelectron spectroscopy is a widely used technique for the analysis of the SEI layer of electrode materials[33,36,44–47]. It enables the investigation of the composition of the passivation layer and can give some insights into amorphous phases that are undetectable by XRD.

The measurements of the as coated electrodes revealed the presence of the Bi-Sb-Te alloy and surface metal oxides. The nanostructured carbon composited presented a larger proportion of surface oxides compared to bulk-BST. The greater volume fraction of amorphous surface oxide shell leads to a thicker and less ion conductive SEI layer[23,48,49]. This in turn significantly hindered sodium ions diffusion, which is reflected in the lower first cycle Coulombic efficiency and the poorer rate capability.

The *ex situ* measurements of fully charged electrode were coupled with ion beam etching which was used to remove some of the SEI layer and acquire stronger signal from the active material. The O 1s, Na 1s, F 1s and C 1s peaks showed differences in composition of the SEI layer. In both electrodes the outermost layer is mainly organic and composed of hydrocarbons. However, ion bombardment revealed that the passivation layer on nano-BST/C electrode possess much higher fraction of inorganic carbonates than in the case of bulk-BST. These results suggest that the SEI of nano-BST/C electrode has a layered structure of an organic outer surface and underneath inorganic electrolyte decomposition products, such as carbonates. Whereas the passivation layer on bulk-BST is mainly composed of more homogeneously distributed inorganics in organic matrix.

The features in the Sb 3d, Te 3d and Bi 4f regions are more pronounced after etching the electrode for 20min. Indeed, some of the peaks are absent in the nano-BST/C before treatment, which again indicates thicker SEI layer. The peak at 571.5 eV confirms presence of $NaTe_3$ in fully charged electrodes. Additionally, in both electrodes peaks associated with Sb and Bi metallic bonds in Bi-Sb mixture were detected[50–52]. In the Sb 3d envelope one more peak can be distinguished at 527.6 eV. It is slightly shifted to lower values from the binding energy of Sb metal and is related to reduced $Sb^{\delta-}$ species indicating Na–Sb bonds[36,47]. Lack of full desodiation of Sb is in accordance with previous reports on antimony-based anodes[36,37,42]. These results confirm formation of a Bi-Sb solid solution. Additionally, as expected, the concentration of Te(0) is relatively higher in the nano-BST/C in agreement with a more facile desodiation of nano-Te. A detailed discussion of the surface analysis is available in the ESI (Fig. S6).

Different behaviour of nanostructured and micron-sized alloy

There are a number of significant points arising from the presented results. First of all, they indicate that the use of a multicomponent alloy is an effective strategy to achieve electrode strengthening against pulverization and consequently enhanced stability. Indeed, the $Bi_{0.25}Sb_{1.75}Te_3$ ternary alloy in both its forms, as a carbon nanocomposite and

as micron-sized powder, shows superior electrochemical performance as compared to its bi-component counterparts Sb_2Te_3 and $Bi_{1-x}Sb_x$ (refer to Fig. S7 for a more detailed comparison of capacity retentions). This is linked to the mechanisms in place during the first sodiation when the $Bi_{0.25}Sb_{1.75}Te_3$ alloy breaks in a unique structure of fine Te particles dispersed in an amorphous Sb-Bi matrix. At higher potentials, when Te is active, the Sb-Bi acts as a buffer to alleviate the volume changes and prevent aggregation to some extent. Such behaviour is reversed at lower potentials where the Sb-Bi matrix plays the major role and Te act as a spectator and simply moderates the continuous expansion and contractions caused by sodiation and desodiation of the active species. These synergic effects between the three components have profound consequences on the overall electrochemical properties and significantly increases the electrode stability over cycling[53].

Even more important is the observation that the effect of Bi substitution is strongly dependant on the particle size of the original alloy. The bulk-BST anode is far more stable and has much higher capacity retention after 100 cycles as compared to the nanosized composite. This phenomenon is counterintuitive, as there is a general consensus, that nanostructuring is generally beneficial for anode materials that exhibit large volume changes upon cycling and, to the best of our knowledge, there are no other reports on better performance of micron-sized materials in comparison to nanostructures[19,54,55].

The different structural stability is even more evident from the SEM images taken after the first charge/discharge cycle for both the bulk-BST and the nano-BST/C electrodes (Fig. 6). In the former, a uniform distribution of small micro-cracks is readily observable. Considering the very low capacity fading (Fig. 3a) these defects don't cause significant loss of electrical contact between active material particles and the current collector. On the other hand, the nano-BST/C electrode shows a larger number of cracks which are also much coarser. The cracks are as wide as 20 µm and hundreds of microns long. It follows that damages caused by volume changes are alleviated much more effectively in the micron-sized alloy relative to the nanosized composite, and hence, it displays a far superior electrochemical performance. Such behaviour is related to the breakage of the original ternary alloy upon the first sodiation which takes different pathways and form different phases depending on the original particle size.

As mentioned before, antimony and bismuth adopt the same crystal structure at fully sodiated state and therefore they can form stable solid solution that can reversibly intercalate sodium ions. While it has not been possible to confirm the presence of the $Bi_{1-x}Sb_x$ solid solution at the end of the first desodiation through *ex situ* XRD measurements, its formation has been observed in the *ex situ* XPS (Fig. 5) measurements and additionally confirmed in the diffraction profile of bulk-BST collected after 50 cycles (Fig. S5). Incorporation of Bi atoms into the Sb lattice leads to solid solution strengthening, which gives electrode material better resistance to internal stresses immediately after the first

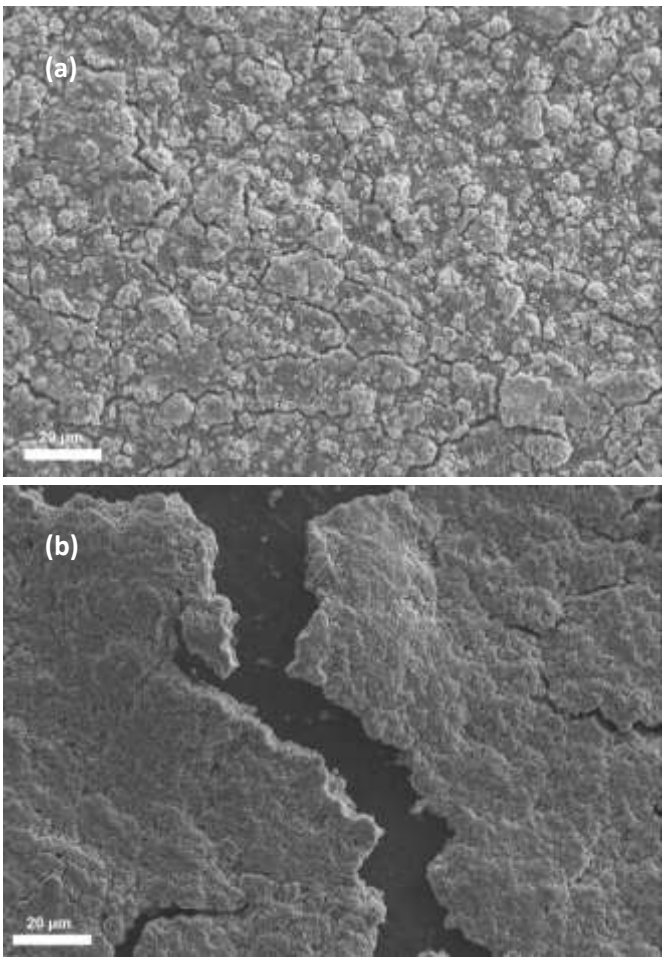

Figure 6. Changes in electrodes morphology after de/sodiation. SEM images of (a) bulk-BST and (b) nano-BST/C electrodes after one full charge/discharge cycle.

sodiation[56]. This appears not to occur in the case of the nanosized powder. Recently it has been reported, that Bi with an average crystallite size of 36 nm forms a high-pressure cubic Na_3Bi phase upon sodiation[43] which therefore could prevent the formation of a solid solution with Sb. The fact that in the bulk-BST electrode solid solution is present and active in different potential than Sb leads to relatively more gradual sodiation, i.e. more sodiation steps, allowing relaxation of some stresses in the material[4]. This buffering effect is less pronounced in the nano material as the Sb-Bi alloy is not stable and Sb segregation occurs. Further experiments aimed at the detailed understanding of the reaction mechanisms as a function of particle size are planned to confirm such scenario.

Electrochemical amorphisation can also depend on particle size, as in the case of lithiation of Si, where it only occurs in micron-sized material in contrast to nano-Si[40]. Analogous differences in de/sodiation mechanism dependent on particle size were reported for various materials[21,40,43], and particularly for Sb[21] where very small size lead to formation of distinct crystalline intermediate phases upon sodiation. Similar behaviour can be expected in the nano-BST/C electrode, where average crystallite size is 6.8 nm. The occurrence of repeated crystallisation events causes an anisotropic stress at

two-phase boundaries, especially at the substrate/electrode interface, which can lead to failure of electrode.

Conclusions

The problem of large volume changes and pulverization occurring in alloy-type anodes strongly hinders their application despite the very attractive gravimetric capacity and electrochemical properties. This issue is rather compelling given that it applies to both Na- and Li-ion batteries. In this work we have shown that it is possible to engineer suitable systems that are highly resistant to fracture without the need of fabricating nanostructures or using encapsulating matrixes. Small substitutions of Sb with Bi in Sb_2Te_3 lead to the ternary alloy $Bi_{0.25}Sb_{1.75}Te_3$ which electrochemical stability is dependent on particle size, with superior performance observed for the bulk micrometre sized material and not when nanosized in a carbon composite. Indeed, bulk $Bi_{0.25}Sb_{1.75}Te_3$ showed high capacity retention (retaining 80% of capacity at high current rate of 2000 mA g^{-1}), enhanced cycling stability and excellent coulombic efficiency. The averaged working potential of $Bi_{0.25}Sb_{1.75}Te_3$ is relatively high, which could lower energy density when employed as anode in full cells. However, in analogy with the commercialised lithium titanates (LTO) chemistries that operate at 1.5 V vs Li, the higher potential avoids issues of Na plating and consequent dendrite formation greatly improving the safe operation of the battery.

A number of experimental techniques were employed to gain insight into the phenomenon and the results indicate that two orders of magnitude difference in particle size influences the reactions mechanisms taking place during sodiation and desodiation. In the bulk powder, the original $Bi_{0.25}Sb_{1.75}Te_3$ breaks during first charging to form Na_2Te, $Na_{3-x}Sb$ and $Na_yBi_{1-x}Sb_x$ phases. However, at the nanoscale the Sb-Bi solid solutions are thought to be unstable and sodiation occurs in the three single elements instead. Furthermore, the particle size has effects on the stability and endurance of the SEI layer which plays a very important role in electrode materials that undergo large volume changes[30,49,59,60]. In the case of the $Bi_{0.25}Sb_{1.75}Te_3$-carbon nanocomposite, the SEI layer is thick and mainly formed by inorganic species resulting in a lower first cycle efficiency and poor rate capability. The high content of inorganic species would make it more susceptible to fracture along grain boundaries, compared to flexible, mainly organic and thinner SEI layer observed in the bulk material.

The large scale production of SIBs is strongly dependant on the availability of highly performing electrode materials which can be manufactured with standard additives using procedures that mimic those already in place for LIBs to achieve easy and cheap drop-in production. $Bi_{0.25}Sb_{1.75}Te_3$ satisfies most of these requirements as electrodes can be prepared directly from the as-made bulk alloy without any particle reduction step, which would greatly increase the production costs. However, the price and availability of the raw main components, especially Te, poses some questions on its effective use in large production. Nevertheless, all the strategies that were put in place in this work to achieve an alloy, which is highly resistant to mechanical fracture when in its bulk form, can drive further research in multicomponent alloys where Te is replaced by one or more sustainable and cost effective elements.

Conflicts of interest

There are no conflicts of interest to declare.

Acknowledgements

SM and MO would like to acknowledge the M2A funding from the European Social Fund via the Welsh Government, the Engineering and Physical Sciences Research Council and Gervaux Ltd. for an EngD bursary to MO. The authors would like to acknowledge funding through the SPECIFIC Innovation and Knowledge Centre (EP/N020863/1), the assistance of the Swansea University AIM facility, which was funded in part by the EPSRC (EO/M028267), the European Regional Development fund through the Welsh Government (80708) and the Sêr Cymru Solar Project via Welsh Government. SM wishes to thank the EPSRC (UK, grant number EP/N013727/1), the National Research Network in Advanced Materials and Manufacturing (Welsh Governament, grant number NRN14) for financial support.

References

1 S. Komaba, W. Murata, T. Ishikawa, N. Yabuuchi, T. Ozeki, T. Nakayama, A. Ogata, K. Gotoh and K. Fujiwara, *Adv. Funct. Mater.*, 2011, **21**, 3859–3867.
2 M. Keller, C. Vaalma, D. Buchholz and S. Passerini, *ChemElectroChem*, 2016, **3**, 1030–1030.
3 M.-S. Balogun, Y. Luo, W. Qiu, P. Liu and Y. Tong, *Carbon N. Y.*, 2016, **98**, 162–178.
4 H. Xie, W. P. Kalisvaart, B. C. Olsen, E. J. Luber, D. Mitlin and J. M. Buriak, *J. Mater. Chem. A*, 2017, **5**, 9661–9670.
5 L. Xiao, Y. Cao, J. Xiao, W. Wang, L. Kovarik, Z. Nie and J. Liu, *Chem. Commun.*, 2012, **48**, 3321.
6 J. Qian, Y. Xiong, Y. Cao, X. Ai and H. Yang, *Nano Lett.*, 2014, **14**, 1865–9.
7 Y. Kim, Y. Kim, A. Choi, S. Woo, D. Mok, N.-S. Choi, Y. S. Jung, J. H. Ryu, S. M. Oh and K. T. Lee, *Adv. Mater.*, 2014, **26**, 4139–44.
8 Y. Zhao and A. Manthiram, *Chem. Mater.*, 2015, **27**, 3096–3101.
9 D. Y. W. Yu, P. V Prikhodchenko, C. W. Mason, S. K. Batabyal, J. Gun, S. Sladkevich, A. G. Medvedev and O. Lev, *Nat. Commun.*, 2013, **4**, 2922.
10 S. Zhu, Q. Li, Q. Wei, R. Sun, X. Liu, Q. An and L. Mai, *ACS Appl. Mater. Interfaces*, 2016, **9**, acsami.6b10143.
11 Y. Zhao and A. Manthiram, *Chem. Mater.*, 2015, **27**, 6139–6145.
12 C. Marino, T. Block, R. Pöttgen and C. Villevieille, *J. Power Sources*, 2017, **342**, 616–622.
13 B. Farbod, K. Cui, W. P. Kalisvaart, M. Kupsta, B. Zahiri, A. Kohandehghan, E. M. Lotfabad, Z. Li, E. J. Luber and D. Mitlin, *ACS Nano*, 2014, **8**, 4415–4429.
14 W. Zhang, J. Mao, W. K. Pang, Z. Guo and Z. Chen, *Electrochim. Acta*, 2017, **235**, 107–113.
15 F. Yang, F. Yu, Z. Zhang, K. Zhang, Y. Lai and J. Li, *Chem. - A Eur. J.*, 2016, n/a-n/a.

16 D. Su, S. Dou and G. Wang, *Nano Energy*, 2015, **12**, 88–95.
17 L. D. Ellis, B. N. Wilkes, T. D. Hatchard and M. N. Obrovac, *J. Electrochem. Soc.*, 2014, **161**, A416–A421.
18 A. Darwiche, C. Marino, M. T. Sougrati, B. Fraisse, L. Stievano and L. Monconduit, *J. Am. Chem. Soc.*, 2012, **134**, 20805–20811.
19 N. Zhang, Y. Liu, Y. Lu, X. Han, F. Cheng and J. Chen, *Nano Res.*, 2015, **8**, 3384–3393.
20 F. Wan, H.-Y. Lü, X.-H. Zhang, D.-H. Liu, J.-P. Zhang, X. He and X.-L. Wu, *J. Alloys Compd.*, 2016, **672**, 72–78.
21 T. Ramireddy, N. Sharma, T. Xing, Y. Chen, J. Leforestier and A. M. Glushenkov, *ACS Appl. Mater. Interfaces*, 2016, **8**, 30152–30164.
22 H. Gao, W. Zhou, J. H. Jang and J. B. Goodenough, *Adv. Energy Mater.*, 2016, **6**, 1–7.
23 M. He, K. Kravchyk, M. Walter and M. V. Kovalenko, *Nano Lett.*, 2014, **14**, 1255–1262.
24 M. Mortazavi, Q. Ye, N. Birbilis and N. V. Medhekar, *J. Power Sources*, 2015, **285**, 29–36.
25 H. Yin, Q. Li, M. Cao, W. Zhang, H. Zhao, C. Li, K. Huo and M. Zhu, *Nano Res.*, 2017, **10**, 2156–2167.
26 S. Liu, J. Feng, X. Bian, J. Liu and H. Xu, *J. Mater. Chem. A*, 2016, **4**, 10098–10104.
27 S. Yuan, X. L. Huang, D. L. Ma, H. G. Wang, F. Z. Meng and X. B. Zhang, *Adv. Mater.*, , DOI:10.1002/adma.201304469.
28 J. Zhang, Y.-X. Yin and Y.-G. Guo, *ACS Appl. Mater. Interfaces*, 2015, **7**, 27838–27844.
29 K.-H. Nam, J.-H. Choi and C.-M. Park, *J. Electrochem. Soc.*, 2017, **164**, A2056–A2064.
30 F. Lin, D. Nordlund, T.-C. Weng, Y. Zhu, C. Ban, R. M. Richards and H. L. Xin, *Nat. Commun.*, 2014, **5**, 3358.
31 N. Yabuuchi, Y. Matsuura, T. Ishikawa, S. Kuze, J.-Y. Y. Son, Y.-T. T. Cui, H. Oji and S. Komaba, *ChemElectroChem*, 2014, **1**, 580–589.
32 L. Ji, M. Gu, Y. Shao, X. Li, M. H. Engelhard, B. W. Arey, W. Wang, Z. Nie, J. Xiao, C. Wang, J. G. Zhang and J. Liu, *Adv. Mater.*, 2014, **26**, 2901–2908.
33 L. O. Vogt, M. El Kazzi, E. Jämstorp Berg, S. Pérez Villar, P. Novák and C. Villevieille, *Chem. Mater.*, 2015, **27**, 1210–1216.
34 H. Lu, L. Wu, L. Xiao, X. Ai, H. Yang and Y. Cao, *Electrochim. Acta*, 2016, **190**, 402–408.
35 M. N. Obrovac, L. Christensen, D. B. Le and J. R. Dahn, *J. Electrochem. Soc.*, 2007, **154**, A849.
36 L. Baggetto, P. Ganesh, C.-N. Sun, R. a. Meisner, T. a. Zawodzinski and G. M. Veith, *J. Mater. Chem. A*, 2013, **1**, 7985.
37 P. K. Allan, J. M. Griffin, A. Darwiche, O. J. Borkiewicz, K. M. Wiaderek, K. W. Chapman, A. J. Morris, P. J. Chupas, L. Monconduit and C. P. Grey, *J. Am. Chem. Soc.*, 2016, **138**, 2352–2365.
38 P. Cucka and C. S. Barrett, *Acta Crystallogr.*, 1962, **15**, 865–872.
39 L. C. Loaiza, E. Salager, N. Louvain, A. Boulaoued, A. Iadecola, P. Johansson, L. Stievano, V. Seznec and L. Monconduit, *J. Mater. Chem. A*, 2017, **5**, 12462–12473.
40 D. Duveau, B. Fraisse, F. Cunin and L. Monconduit, *Chem. Mater.*, 2015, **27**, 3226–3233.
41 W. J. Zhang, *J. Power Sources*, 2011, **196**, 877–885.
42 L. Baggetto, H.-Y. Hah, J.-C. Jumas, C. E. Johnson, J. A. Johnson, J. K. Keum, C. A. Bridges and G. M. Veith, *J. Power Sources*, 2014, **267**, 329–336.
43 J. Sottmann, M. Herrmann, P. Vajeeston, Y. Hu, A. Ruud, C. Drathen, H. Emerich, H. Fjellvåg and D. S. Wragg, *Chem. Mater.*, 2016, acs.chemmater.6b00491.
44 M. A. Muñoz-Márquez, M. Zarrabeitia, E. Castillo-Martínez, A. Eguía-Barrio, T. Rojo and M. Casas-Cabanas, *ACS Appl. Mater. Interfaces*, 2015, **7**, 7801–7808.
45 A. Darwiche, L. Bodenes, L. L. Madec, L. Monconduit and H. Martinez, *Electrochim. Acta*, 2016, **207**, 284–292.
46 F. Klein, R. Pinedo, P. Hering, A. Polity, J. J. Janek and P. Adelhelm, *J. Phys. Chem. C*, 2016, **120**, 1400–1414.
47 L. Baggetto, E. Allcorn, A. Manthiram and G. M. Veith, *Electrochem. commun.*, 2013, **27**, 168–171.
48 K. He, F. Lin, Y. Zhu, X. Yu, J. Li, R. Lin, D. Nordlund, T. C. Weng, R. M. Richards, X. Q. Yang, M. M. Doeff, E. A. Stach, Y. Mo, H. L. Xin and D. Su, *Nano Lett.*, 2015, **15**, 5755–5763.
49 L.-Y. Kuo, A. Moradabadi, H.-F. Huang, B.-J. Hwang and P. Kaghazchi, *J. Power Sources*, 2017, **341**, 107–113.
50 S. Aminorroaya-Yamini, C. Zhang, X. Wang and I. Nevirkovets, *J. Phys. D. Appl. Phys.*, 2012, **45**, 125301.
51 H.-Y. Cheng, C. A. Jong, R.-J. Chung, T.-S. Chin and R.-T. Huang, *Semicond. Sci. Technol.*, 2005, **20**, 1111–1115.
52 F. Wei, L. Wang, T. Kong, L. Shi, R. Huang, J. Zhang and G. Cheng, *Appl. Phys. Lett.*, 2013, **103**, 2–6.
53 J. Qian, Y. Xiong, Y. Cao, X. Ai and H. Yang, *Nano Lett.*, 2014, **14**, 1865.
54 Y. Liu, N. Zhang, L. Jiao, Z. Tao and J. Chen, *Adv. Funct. Mater.*, 2015, **25**, 214–220.
55 Y. Liu, N. Zhang, L. Jiao and J. Chen, *Adv. Mater.*, 2015, **27**, 6702–6707.
56 Z. Du, T. D. Hatchard, R. A. Dunlap and M. N. Obrovac, *J. Electrochem. Soc.*, 2015, **162**, A1858–A1863.
57 K. Xu, *Chem. Rev.*, 2004, **104**, 4303–4418.
58 U. Boesenberg, M. a. Marcus, A. K. Shukla, T. Yi, E. McDermott, P. F. Teh, M. Srinivasan, A. Moewes and J. Cabana, *Sci. Rep.*, 2014, **4**, 7133.